

UniRain: Unified Image Deraining with RAG-based Dataset Distillation and Multi-objective Reweighted Optimization

Qianfeng Yang¹ Qiyuan Guan¹ Xiang Chen² Jiyu Jin^{1*} Guiyue Jin¹ Jiangxin Dong²

¹Dalian Polytechnic University ²Nanjing University of Science and Technology

<https://lowlevelcv.com/> <https://github.com/QianfengY/UniRain>

Abstract

Despite significant progress has been made in image deraining, we note that most existing methods are often developed for only specific types of rain degradation and fail to generalize across diverse real-world rainy scenes. How to effectively model different rain degradations within a universal framework is important for real-world image deraining. In this paper, we propose UniRain, an effective unified image deraining framework capable of restoring images degraded by rain streak and raindrop under both daytime and nighttime conditions. To better enhance unified model generalization, we construct an intelligent retrieval augmented generation (RAG)-based dataset distillation pipeline that selects high-quality training samples from all public deraining datasets for better mixed training. Furthermore, we incorporate a simple yet effective multi-objective reweighted optimization strategy into the asymmetric mixture-of-experts (MoE) architecture to facilitate consistent performance and improve robustness across diverse scenes. Extensive experiments show that our framework performs favorably against the state-of-the-art models on our proposed benchmarks and multiple public datasets.

1. Introduction

Recent years have witnessed the emergence of diverse rain datasets [1, 16, 17] and the development of numerous deep learning-based deraining methods [4, 18, 35]. As the field has evolved, researchers have increasingly focused on addressing different rain degradation patterns, such as rain streaks [48], raindrops [30], nighttime rain [13], and so on. Such clear settings enable researchers to build models adapted to the specific characteristics of each rainy scenario.

However, these models are typically designed for specific rain degradation patterns, and their performance often drops significantly when applied to other types of rain. Real-world rainy scenes are highly complex and dynamic. For example, daytime rain is mainly characterized by streak degradations, while nighttime scenes, affected by low illu-

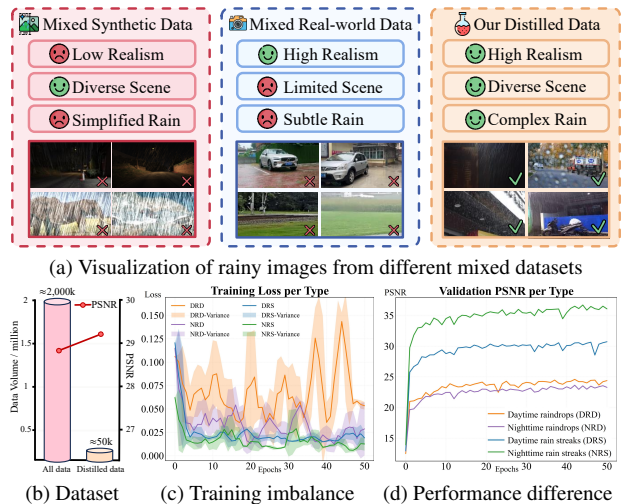


Figure 1. Overview of **motivation**. (a) Rainy image samples from public datasets, illustrating the noticeable differences in data quality. (b) Directly merging existing synthetic and real datasets enlarges data volume, yet quality disparity hinders performance, as shown by PSNR results. (c) The loss curves of DRS, DRD, NRS, and NRD (denoting daytime/nighttime rain streaks and raindrops) show different convergence rates, leading to imbalance in unified training. (d) The PSNR curves indicate that the model tends to favor simpler degradations but struggles with complex ones.

mination and varying light sources, amplify the complexity of rain artifacts. Intelligent systems need to handle multiple rain degradation types, but relying on separate models for different conditions makes switching cumbersome and significantly reduces deployment efficiency [19, 23, 45]. However, few effort has been made in unified image deraining due to the absence of mixed datasets that integrate multiple rain degradation types. Thus, it is of great interest to unlock a unified image deraining method that can simultaneously handle multiple rain degradations within a single model.

To achieve better unified image deraining, two key factors should be considered: constructing mixed dataset and designing unified model. Regarding the **mixed dataset**, the most direct strategy is to merge all synthetic and real-world rain datasets (*i.e.*, > 2,000k pairs) [17, 30, 31, 48, 52].

However, we note that these public datasets vary noticeably in quality, as some visual samples illustrated in Figure 1a. Such uneven data quality may lead to introduce inaccurate supervisory signals during training, which hinders model convergence [27]. This instability further causes undesirable interference and weakens the model’s ability to generalize across diverse rain conditions, as shown in Figure 1b. These insights motivate us to distill reliable data from large-scale public datasets for unified image deraining.

For the **unified model**, how to equip it with consistent capability across diverse rain conditions is of vital importance. As depicted in Figure 1c, we find that different types of rain degradations exhibit varying levels of difficulty and distinct convergence behaviors during training. If we train mixed rain-type data with the same optimization objective, it would lead to imbalance across different degradation types [11]. In this case, the model tends to overfit easier rain types (*e.g.*, nighttime rain streaks) while struggling with more complex rain degradations (*e.g.*, daytime raindrops), resulting in uneven restoration quality, as illustrated in Figure 1d. This motivates us to introduce a multi-objective optimization strategy to balance the deraining capability of the unified model across different rain types.

To address these issues, we propose UniRain, an effective unified image deraining framework capable of restoring images degraded by rain streak and raindrop under both daytime and nighttime conditions. Specifically, we first construct an intelligent retrieval augmented generation (RAG)-based dataset distillation pipeline that distills reliable training samples from all public deraining datasets for better mixed training. We build a database of real-world rainy images to guide vision-language models (VLMs) in assessing data quality, thereby enabling large-scale dataset evaluation and distillation of high-quality samples for unified image deraining. Furthermore, we develop an asymmetric mixture-of-experts (MoE) architecture, where the encoder integrates the soft-MoE to collaboratively preserve diverse degradation cues, while the decoder employs the hard-MoE with top-k routing to enhance fine texture reconstruction. To achieve better training balance, we incorporate a simple yet effective multi-objective reweighted optimization strategy into the framework to harmonize the learning of different rain degradation types. Extensive experiments demonstrate that our framework performs consistently favorably against the state-of-the-art models on both our proposed benchmarks and multiple public datasets.

We summarize our main contributions as follows:

- We propose UniRain, an effective unified image deraining model capable of handling rain streaks and raindrops under daytime and nighttime conditions.
- We develop an intelligent RAG-based data distillation pipeline that filters reliable training samples from public datasets to improve training on mixed data.

- We introduce a simple yet effective multi-objective reweighted optimization strategy to harmonize the learning of multiple types and alleviate task imbalance.
- Extensive experiments demonstrate that our UniRain achieves consistently competitive performance in terms of both quantitative metrics and visual quality.

2. Related Work

Deep image deraining. In recent years, the field of single image deraining has witnessed the emergence of numerous approaches and benchmark datasets [7]. With respect to **deraining datasets**, numerous synthetic datasets featuring different types of rain degradation have been proposed, including rain streaks (*e.g.*, Rain200L/H [48], Rain13k [17]), raindrops (*e.g.*, RainDrop [30], RainDS [31]), and nighttime rain (*e.g.*, GTAV-NightRain [52], HQ-NightRain [13]). To boost real-world deraining performance, several real-world datasets have been proposed, including SPA-Data [40], GT-Rain [1], and LHP-Rain [16]. It is worth noting that significant differences exist among these datasets in terms of background quality, image resolution, and the formation patterns of rain. In this work, we propose a dataset distillation strategy to select high-quality training samples from all public datasets, aiming to better facilitate unified image deraining.

Regarding the **deraining models**, we note that most existing approaches remain limited to handling only specific types of rain degradation, without considering a unified solution that generalizes across diverse real-world rainy scenarios. Inspired by the concept of all-in-one image restoration, Yan first contributed a universal deraining network developed for multiple rain degradation types in driving scenarios [45]. To break through the generalization bottleneck of image deraining, our goal is to develop a unified deraining framework capable of simultaneously handling multiple rain degradation types across diverse real-world scenarios.

Retrieval augmented generation (RAG). RAG refers to the process of retrieving relevant information from external knowledge bases prior to generating outputs with large language models (LLMs) [21]. This allows models to leverage domain-specific information and generate more informed outputs without requiring retraining [10]. As a cutting-edge technique, it has been applied in high-level vision tasks, *e.g.*, image analysis [25, 54], image synthesis [2, 28], and 3D modeling [41, 47]. Recent studies have begun exploring the potential of RAG in low-level vision tasks. For example, Guo *et al.* [15] proposed ReFIR, a training-free retrieval-augmented image restoration framework that retrieves content-relevant high-quality references and injects them into large restoration models to boost fidelity. Inspired by this popular technique, we first leverage RAG in the process of dataset distillation to better facilitate model training.

Multi-objective learning. Multi-objective learning jointly optimizes models across multiple tasks, leveraging shared

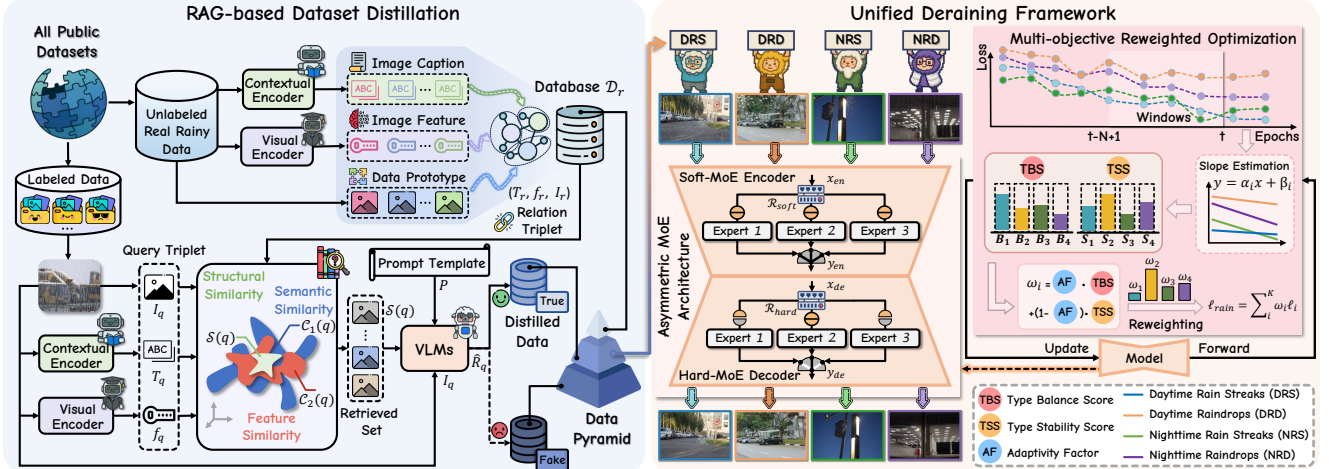


Figure 2. Overall framework of **UniRain**. (Left) The RAG-based dataset distillation pipeline retrieves real rainy references consistent with the query image via multi-level similarity search and employs vision language models to evaluate its quality, thereby distilling reliable samples from public datasets. (Right) The asymmetric MoE architecture consists of soft-MoE encoder and hard-MoE decoder, optimized via the multi-objective reweighted strategy to achieve balanced learning and robust performance across multiple rain degradation types.

representations to capture common underlying structures among related tasks [9]. In the context of optimizing multiple objectives that may exhibit conflicting gradients, multi-objective learning has been extensively investigated to improve both optimization stability and overall task performance. To this end, numerous techniques have been proposed, including multi-armed bandit [34], gradient manipulation approaches [49] and self-paced learning [20]. For low-level vision tasks, Sun *et al.* [36] proposed a hybrid evolutionary gradient optimizer to balance perceptual quality and reconstruction fidelity through multi-objective optimization. In this work, we propose a dynamic reweighted optimization mechanism to adaptively balance multiple rain degradation removal objectives for unified image deraining.

3. Methodology

Our goal is to formulate an effective unified image deraining model that can address multiple types of rain degradations. Towards this goal, we develop an intelligent RAG-based dataset distillation pipeline that evaluates large-scale public datasets and selects high-quality samples for more balanced mixed training, as illustrated in Figure 2 (left). Furthermore, to achieve consistent performance and improved robustness, we incorporate a simple yet effective multi-objective reweighted optimization strategy into the asymmetric MoE architecture, as shown in Figure 2 (right). In what follows, we present the details of the proposed approach.

3.1. RAG-based dataset distillation

If all synthetic and real datasets are directly mixed for training, the uneven data quality may introduce interference and consequently degrade the model performance. To maximize the effectiveness of mixed training dataset, we construct

the RAG-based dataset distillation pipeline. The pipeline mainly consists of retrieval stage, which retrieves relevant real-world reference, and generation stage, which assesses data quality and distills reliable samples for training.

Retrieval stage. This stage start from a large-scale knowledge corpus of millions of synthetic and real rainy images, partitioned into unlabeled real data for database construction and labeled data for distillation. For each real image I_r , a textual caption T_r is generated using the contextual encoder BLIP [24], and a visual encoder CLIP [32] is used to extract its feature embedding f_r . The resulting relation triplet (T_r, f_r, I_r) is then stored in the database \mathcal{D}_r . For each query image, we perform a similar process [12, 24, 46] to obtain its relation triplet (T_q, f_q, I_q) . Given the query triplet, we adopt a hierarchical similarity matching process that considers semantic, feature, and structural similarities to retrieve the most relevant samples from \mathcal{D}_r . Specifically, we first compute the semantic similarity score $s_{txt}(q, r)$:

$$s_{txt}(q, r) = \|\phi_T(T_q) - \phi_T(T_r)\|_2, \quad (1)$$

where $\phi_T(\cdot)$ denotes the CLIP text encoder and $\|\cdot\|_2$ denotes the L_2 norm. The top K_1 samples with the highest semantic similarity scores form the initial candidate set $\mathcal{C}_1(q)$. Within this candidate set, we further compute the visual feature similarity scores $s_{vis}(q, r')$ using cosine similarity to assess appearance closeness, as defined below:

$$s_{vis}(q, r') = \frac{f_q^\top f_{r'}}{\|f_q\|_2 \|f_{r'}\|_2}, \quad r' \in \mathcal{C}_1(q). \quad (2)$$

The candidate set $\mathcal{C}_2(q)$ is constructed, retaining the top K_2 most similar samples. Finally, we employ the $SSIM(\cdot)$

function to evaluate structural similarity and capture fine-grained perceptual consistency, as defined below:

$$s_{perc}(q, r'') = SSIM(I_q, I_{r''}), \quad r'' \in \mathcal{C}_2(q). \quad (3)$$

The top K_3 samples are selected based on the structural similarity scores $s_{perc}(q, r'')$ to construct $\mathcal{S}(q)$. Through this hierarchical similarity matching process, the pipeline ensures that $\mathcal{S}(q)$ contains the most semantically and visually consistent real rainy scenes, which serve as authentic references for data distillation.

Generation stage. Once the retrieved set $\mathcal{S}(q)$ is obtained, it is combined with the query image I_q and a predefined prompt template P as input to the VLMs. The overall generation process is expressed as follows:

$$R_q = \mathcal{V}(I_q, \mathcal{S}(q), P), \quad (4)$$

where $\mathcal{V}(\cdot)$ is the VLM, and R_q represents the VLM’s response. To enhance reliability, we adopt an ensemble voting strategy across three independent VLMs (InternVL2.5-8B [8], LLaVA-NeXT-7B [22], and MobileVLM-3B [43]). Let $R_q^i \in \{0, 1\}$ denote the binary response from the i -th model, where 1 indicates True and 0 indicates False. The final decision is determined by majority voting:

$$\hat{R}_q = \begin{cases} 1 & \text{if } \sum_{i=1}^3 \mathbb{I}(R_q^i = 1) \geq 2, \\ 0 & \text{otherwise,} \end{cases} \quad (5)$$

where $\mathbb{I}(\cdot)$ is the indicator function, and $\hat{R}_q = 1$ indicates the query rainy image is considered reliable. Finally, this process forms a data-quality pyramid, where the top layer represents real rainy data, the middle layer consists of distilled high-quality and reliable data close to real distributions, and the bottom layer contains low-fidelity samples. Through this hierarchical refinement, the system distills millions of images into a reliable dataset.

3.2. Multi-objective reweighted optimization

Training a single model to jointly handle different rain types introduces optimization imbalance. The shared optimization objective tends to favor easier rain type with faster loss decay, while more difficult ones remain under-optimized. Consequently, the learned representations become biased, limiting the model’s overall generalization across diverse degradations. To address the above imbalance, we propose multi-objective reweighted optimization, an adaptive strategy inspired by [11], which dynamically balances convergence rates and harmonizes multi-objective optimization during training. This strategy consists of convergence slope estimation, which estimates each type’s convergence rate through linear regression of loss, and adaptive reweighting, which integrates type balance score (TBS), type stability score (TSS), and adaptivity factor (AF), to dynamically balance type contributions and maintain stable optimization.

Convergence slope estimation. We first estimate the convergence tendency of each type by analyzing the evolution of its loss. Let $\{(k, y_k)\}_{k=t-N+1}^t$ denote the training-step indices and their corresponding normalized losses within a sliding window $[t - N + 1, t]$, where N is the window size and t is the current iteration. To capture short-term convergence dynamics, we apply a least-squares linear fitting over this window and define the regression coefficient α as the convergence slope, which measures the local rate of loss change. The slope and intercept are calculated as:

$$\alpha = \frac{\sum_{k=1}^N (k - \bar{k})(y_k - \bar{y})}{\sum_{k=1}^N (k - \bar{k})^2}, \quad \beta = \bar{y} - \alpha \bar{k}, \quad (6)$$

where $\bar{k} = \frac{1}{N} \sum_{k=t-N+1}^t k$ and $\bar{y} = \frac{1}{N} \sum_{k=t-N+1}^t y_k$ are the mean values within the window. In this definition, $\alpha < 0$ indicates a decreasing loss (converging), $\alpha > 0$ implies divergence, and a larger $|\alpha|$ denotes a faster change rate.

Adaptive reweighting. This estimated slope α serves as the foundation for computing the subsequent adaptive weighting indicators, namely type balance score (TBS), type stability score (TSS), and adaptivity factor (AF), which jointly determine how type weights evolve during training. The goal of TBS is to assign smaller weights to types that converge faster and larger weights to those that converge more slowly, ensuring synchronized convergence among all types. For each type i at iteration t , we define the TBS as

$$\text{TBS}_i(t) = \text{softmax}_i \left(K \frac{\alpha_i(t)}{\sum_{i=1}^K |\alpha_i(t)|} \right), \quad (7)$$

where $\alpha_i(t)$ is the convergence slope of type i , softmax_i operates across the type dimension, and K denotes the total number of degradation types. This normalization removes scale sensitivity and ensures that slower types obtain higher TBS values, thus receiving greater optimization emphasis.

However, relying solely on TBS is insufficient, since a diverging type with a large positive slope could still obtain an undesirably high score. To mitigate this issue, we propose the TSS, which evaluates each type’s internal stability by considering its historical convergence behavior:

$$\text{TSS}_i(t) = \text{softmax}_i \left(-N \frac{\alpha_i(t)}{\sum_{k=t-N+1}^t |\alpha_i(k)|} \right), \quad (8)$$

where normalization is performed along the temporal dimension k from step $t - N + 1$ to t , but subsequently applies the softmax function across the type dimension i . A higher TSS indicates stable and consistent convergence, whereas diverging types receive lower scores.

During early training, all types generally exhibit convergent behavior, in which case TBS should dominate the weighting process. As training proceeds, some types may

begin to diverge and thus require greater influence from TSS. To achieve a transition between these two regimes, we define the AF that reflects the global divergence state:

$$\text{AF}(t) = \min\left(t \cdot \text{softmax}_t\left(-\frac{\tau t \cdot \alpha_{\max}(t)}{\sum_{i=1}^t \alpha_{\max}(i)}\right), 1\right), \quad (9)$$

where $\alpha_{\max}(t)$ is the largest convergence slope across all types and softmax_t is applied along the temporal dimension. The term t prevents AF from monotonically decreasing as training progresses, while τ controls its sensitivity. Finally, the type loss weights are defined as follows:

$$\omega_i(t) = \text{AF}(t) \text{TBS}(t) + (1 - \text{AF}(t)) \text{TSS}(t), \quad i \in [1, K] \quad (10)$$

where $\omega_i(t)$ is the dynamic weight vector across K rain types. This approach enables adaptive focus between inter-type balance and intra-type stability, ensuring steady convergence and improved generalization across all rain types.

3.3. Asymmetric MoE architecture

To address diverse rain degradation behaviors, we adopt an asymmetric MoE with the soft-MoE encoder and the hard-MoE decoder for adaptive and efficient processing.

Soft-MoE encoder. Given an input feature x_{en} , the soft router function \mathcal{R}_{soft} generates continuous routing weights to adaptively combine multiple experts:

$$\mathcal{R}_{soft} = \sigma(\mathcal{W}(\varphi(x_{en} + \epsilon))), \quad (11)$$

where $\mathcal{W}(\cdot)$ is a learnable projection, $\varphi(\cdot)$ is global average pooling, $\epsilon \sim \mathcal{N}(0, \sigma^2)$ is the Gaussian noise for load balancing, and $\sigma(\cdot)$ is the softmax. The output y_{en} combines all experts contributions through weighted aggregation:

$$y_{en} = \sum_{i=1}^N \mathcal{R}_{soft}^i \otimes y_{en}^i, \quad (12)$$

where \otimes is the element-wise multiplication, y_{en}^i is the feature produced by the i -th expert, \mathcal{R}_{soft}^i is the routing weight of the i -th expert, and N is the total number of experts.

Hard-MoE decoder. For the decoder input x_{de} , the hard router \mathcal{R}_{hard} function selectively activates the most relevant experts via Top- k routing. The process is defined as:

$$\mathcal{R}_{hard} = \mathcal{T}_k(\sigma(\mathcal{W}(\varphi(x_{de} + \epsilon)))), \quad (13)$$

$$y_{de} = \sum_{i=1}^N \mathcal{R}_{hard}^i \cdot y_{de}^i, \quad (14)$$

where $\mathcal{T}_k(\cdot)$ denotes the Top- k selection operator and y_{de}^i is the output of the i -th decoder expert. This design enables the hard-MoE to efficiently allocate computation to the most relevant experts, focusing on structural and fine-grained detail reconstruction, and complementing the soft-MoE encoder for balanced expressiveness and efficiency.

4. Experiments

4.1. Experimental settings

Training dataset. Through the RAG-based dataset distillation pipeline, we construct RainRAG, a high-quality dataset distilled from large-scale (*i.e.*, $> 2,000k$ pairs) public synthetic and real-world deraining datasets [1, 3, 13, 16, 17, 30, 31, 40, 42, 45, 48, 52]. Our pipeline retains approximately 2.6% of the original data, ensuring only high-quality samples for model training. The training set consists of 52,869 pairs and divided into four representative subsets: daytime rain streaks (DRS), daytime raindrops (DRD), nighttime rain streaks (NRS), and nighttime raindrops (NRD).

Test datasets. To comprehensively evaluate our model’s capability in unified image deraining, we obtain 400 test image pairs using the same filtering process and evenly divide them into four subsets: DRS, DRD, NRS, and NRD. In addition, we evaluate our method alongside other comparison methods on several real-world benchmarks (*i.e.*, RealRain-1k [26], RainDS-real [31], and WeatherBench [14]).

Implementation details. We train our proposed UniRain on 4 NVIDIA GeForce RTX 4090 GPUs using the AdamW optimizer with default parameters. During training, images are randomly cropped into 128×128 patches with a batch size of 8. The initial learning rate is set to 2×10^{-4} and gradually reduces to 1×10^{-6} using a cosine annealing scheduler. For the asymmetric MoE architecture, each expert is designed with a distinct self-attention capacity, enabling diverse feature modeling across varying attention complexities. We train the network for a total of 300,000 iterations. For multi-objective reweighted optimization, we set the step window size to 10 and the sensitivity parameter τ to 5.

4.2. Comparison with the state-of-the-art

We compare our proposed UniRain with 10 image deraining technologies, including PReNet [33], RCDNet [39], MPRNet [50], Restormer [51], IDT [44], DRSformer [5], RLP [53], MSDT [4], NeRD-Rain [6], and URIR [45].

Evaluation on the RainRAG dataset. Table 1 shows that the proposed UniRain achieves the best average performance across four rain degradation types. Compared with Restormer [51] and NeRD-Rain [6], it achieves improvements of 1.35 dB and 1.41 dB in PSNR on the DRD subset, respectively. As shown in Figure 3, we further present the visual comparisons under various rain degradations, where our method delivers superior deraining performance. In contrast, other methods still exhibit rain streak residuals and fail to recover background details affected by raindrops.

Evaluation on real-world public benchmarks. For further general verification in practical applications, we conduct comparisons with other methods on the real-world rainy datasets. As shown in Table 2, our method achieves the best

Table 1. Quantitative evaluations on the proposed RainRAG dataset, where DRS, DRD, NRS, and NRD denote daytime rain streaks, daytime raindrops, nighttime rain streaks, and nighttime raindrops, respectively. The best and second-best values are **bold** and underlined.

Datasets		RainRAG Dataset														
Methods	Venue	DRS			DRD			NRS			NRD			Average		
		PSNR \uparrow	SSIM \uparrow	LPIPS \downarrow	PSNR \uparrow	SSIM \uparrow	LPIPS \downarrow	PSNR \uparrow	SSIM \uparrow	LPIPS \downarrow	PSNR \uparrow	SSIM \uparrow	LPIPS \downarrow	PSNR \uparrow	SSIM \uparrow	LPIPS \downarrow
LQ	-	23.79	0.7514	0.3207	20.79	0.7293	0.2433	26.89	0.8480	0.3583	21.05	0.5590	0.6130	23.13	0.7220	0.3839
PReNet [33]	CVPR 2019	26.73	0.8233	0.1885	21.45	0.7358	0.2697	32.85	0.9520	0.1957	24.29	0.8058	0.3751	26.33	0.8292	0.2572
RCDNet [39]	CVPR 2020	25.27	0.7949	0.2777	21.46	0.7295	0.2778	28.44	0.9070	0.2996	20.62	0.5832	0.5931	23.95	0.7537	0.3620
MPRNet [50]	CVPR 2021	27.99	0.8242	<u>0.1701</u>	22.50	0.7264	0.3308	33.75	0.9541	0.1834	24.46	0.8118	0.3634	27.17	0.8291	0.2619
Restormer [51]	CVPR 2022	28.45	0.8298	0.1725	<u>23.36</u>	0.7547	0.2323	33.92	0.9541	0.1830	<u>25.85</u>	0.8234	0.3452	27.89	0.8405	<u>0.2332</u>
IDT [44]	TPAMI 2022	26.97	0.8279	0.1960	23.17	<u>0.7648</u>	0.2300	33.05	0.9470	0.2132	25.20	0.7963	0.3718	27.10	0.8340	0.2527
DRSformer [5]	CVPR 2023	28.08	0.8253	0.1960	22.93	0.7499	0.2407	32.86	0.9457	0.2202	24.99	0.7953	0.3702	27.22	0.8291	0.2568
RLP [53]	ICCV 2023	28.01	0.8290	0.2339	22.42	0.7353	0.3029	32.06	0.9438	0.1971	23.48	0.7638	0.4282	26.49	0.8180	0.2905
MSDT [4]	AAAI 2024	<u>28.60</u>	0.8414	0.1576	23.31	0.7487	0.2587	<u>34.56</u>	<u>0.9591</u>	<u>0.1677</u>	25.28	0.8148	0.3555	<u>27.94</u>	0.8410	0.2349
NeRD-Rain [6]	CVPR 2024	28.11	0.8309	0.1720	23.30	0.7513	<u>0.2318</u>	33.88	0.9511	0.1964	25.31	0.8027	0.3571	27.65	0.8340	0.2393
URIR [45]	AAAI 2025	28.29	0.8386	0.2001	23.19	0.7483	0.2815	34.32	0.9570	0.1860	25.82	<u>0.8263</u>	<u>0.3390</u>	27.91	<u>0.8425</u>	0.2516
UniRain (Ours)	-	29.58	<u>0.8400</u>	0.1814	24.71	0.7687	0.2408	35.23	0.9592	0.1617	26.21	0.8380	0.3275	28.93	0.8515	0.2279

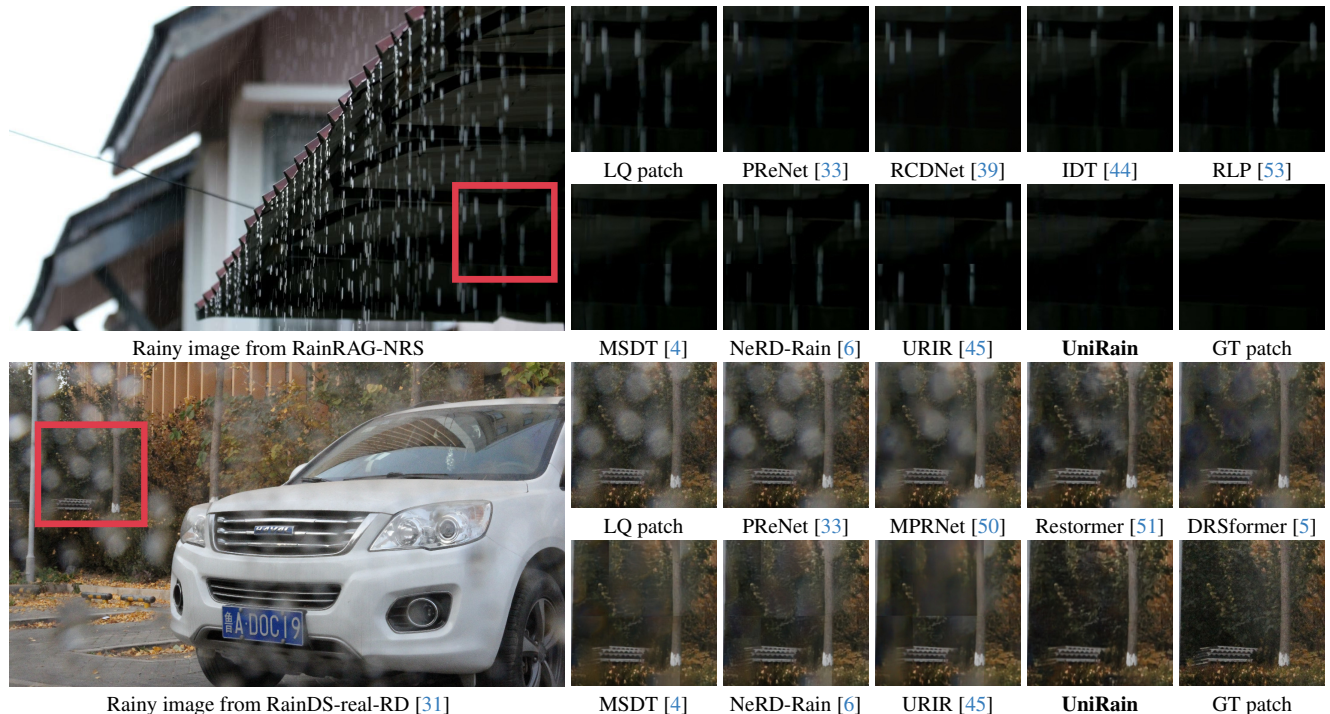


Figure 3. Visual comparison of image deraining results on the RainRAG-NRS and RainDS-real-RD datasets. Zoom in for a better view.

overall performance, outperforming URIR [45] by 1.73 dB in PSNR on average. Figure 4 shows that our method not only removes real and complex rain streaks but also restores clear details, even achieving visually better results than the GT by eliminating residual raindrops contained in it.

Generalization to multiple application scenarios. We further evaluate the generalization ability of our method across multiple application scenarios, including autonomous driving, unmanned aerial vehicle (UAV), and maritime scenes. As presented in Figure 5, other methods struggle to preserve pixel-level structural fidelity, whereas our method produces faithful and visually pleasing results, demonstrating generalization across multiple scenarios.

Model complexity. We evaluate the complexity of our method and state-of-the-art ones in terms of FLOPs and

Params. As shown in Table 3, UniRain achieves competitive performance with lower FLOPs and fewer parameters.

4.3. Analysis and discussion

Effectiveness of RAG-based dataset distillation. We first analyze the impact of different mixed training datasets on the performance of the unified deraining model, including (1) synthetic dataset combinations, (2) real-world dataset combinations, and (3) synthetic & real dataset combinations. As shown in Figure 6a, we present the quantitative results of the same model trained on these equal-sized dataset combinations across four rain types. It can be observed that the model trained with our distilled dataset achieves the best overall performance, surpassing all other dataset combinations. Figure 6b visualizes the corresponding feature distri-

Table 2. Quantitative evaluations on the real-world public benchmarks. The best and second-best values are **bold** and underlined.

Datasets	Metrics	PRNet [33]	RCDNet [39]	MPRNet [50]	IDT [44]	Restormer [51]	DRSformer [5]	RLP [53]	MSDT [4]	NeRD-Rain [6]	URIR [45]	UniRain (Ours)
RealRain-1k-L [26]	PSNR ↑	28.80	28.58	33.89	33.71	32.44	33.65	32.02	33.56	<u>33.98</u>	33.54	36.51
	SSIM ↑	0.9307	0.9202	0.9701	0.9664	0.9644	0.9625	0.9558	0.9640	<u>0.9710</u>	0.9686	0.9778
RealRain-1k-H [26]	PSNR ↑	25.49	25.46	30.83	30.37	28.80	30.35	29.01	30.91	<u>31.37</u>	31.10	33.74
	SSIM ↑	0.8820	0.8613	0.9542	0.9441	0.9389	0.9360	0.9309	0.9451	<u>0.9583</u>	0.9550	0.9672
RainDS-real-RD [31]	PSNR ↑	19.08	19.37	19.48	20.35	20.74	20.15	20.86	20.72	<u>21.01</u>	20.44	22.07
	SSIM ↑	0.6020	0.5937	0.5957	0.6237	<u>0.6346</u>	0.6133	0.6136	0.6205	0.6155	0.5945	0.6436
RainDS-real-RDS [31]	PSNR ↑	18.21	18.57	18.74	18.98	19.13	18.79	19.85	19.36	<u>19.93</u>	19.87	20.61
	SSIM ↑	0.5665	0.5572	0.5681	0.5833	<u>0.5876</u>	0.5712	0.5762	0.5830	0.5839	0.5689	0.5881
WeatherBench-rain [14]	PSNR ↑	31.18	27.91	32.35	32.05	32.91	31.90	31.48	<u>33.56</u>	32.77	33.50	34.25
	SSIM ↑	0.9364	0.8880	0.9352	0.9355	0.9372	0.9281	0.9330	0.9453	0.9372	0.9435	<u>0.9448</u>
Average	PSNR ↑	24.55	23.98	27.06	27.09	26.80	26.97	26.64	27.62	<u>27.81</u>	27.69	29.42
	SSIM ↑	0.7835	0.7641	0.8047	0.8106	0.8125	0.8022	0.8019	0.8116	<u>0.8132</u>	0.8061	0.8222



Figure 4. Visual comparison of image restoration results on the real-world benchmark (*i.e.*, WeatherBench [14]). Compared to the state-of-the-art methods, our UniRain restores a high-quality image with clear details, even outperforming the GT by removing residual raindrops.

Table 3. Comparisons of model complexity against state-of-the-art methods. The size of the test image is 256×256 pixels.

Methods	Restormer [51]	DRSformer [5]	NeRD-Rain [6]	UniRain (Ours)
FLOPs (G)	140.990	220.378	147.978	126.541
Params (M)	26.097	33.627	22.856	24.388

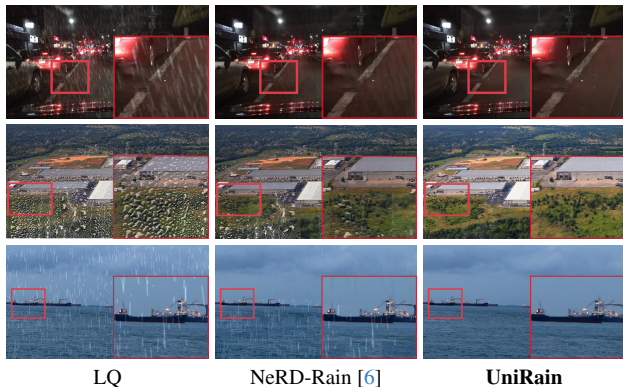
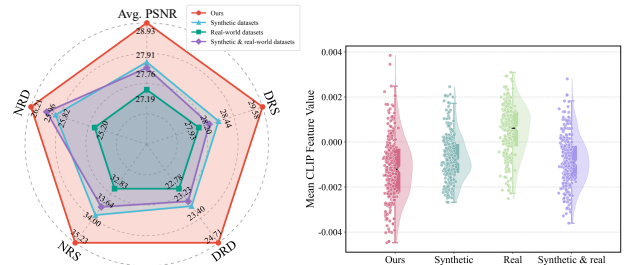


Figure 5. Generalization results across multiple scenarios. Our method achieves the best restoration results in driving scenes (first row), UAV scenes (second row), and maritime scenes (third row).

butions, revealing that our distilled dataset covers a wider and more diverse feature space. This richer representation contributes to stronger generalization ability and ensures more consistent deraining performance across diverse rain conditions. Besides, we compare the averaged results between directly mixing all synthetic and real-world datasets and using our distilled dataset on the test set of Table 2. As shown in Figure 1b, directly combining all datasets for training leads to suboptimal results due to inconsistent data quality across different sources. This finding indicates that simply enlarging the dataset does not necessarily lead to better generalization. Rather, the reliability and quality of



(a) Different combination strategies

(b) Feature distributions

Figure 6. Statistical ablation analysis of different combination strategies and their feature distributions across combinations.

the data are the key factors that dictate model performance.

Finally, to further validate the effectiveness of our proposed RAG-based dataset distillation pipeline, we conduct a comparison with several ablated variants, including (i) using only VLMs without RAG, (ii) without retrieval stage, and (iii) without generation stage. As shown in Table 4, our designed pipeline obtains higher performance as it leverages real-scene images to filter training data, ensuring that high-quality samples are distilled for model training.

Effectiveness of multi-objective reweighted optimization. We compare our multi-objective reweighted optimization strategy with alternative schemes, including continual learning (*e.g.*, PIGWM [55]) and prompt learning (*e.g.*, PromptIR [29]). We conduct experiments on the RainDS-real-RDS [31] dataset, with the quantitative results shown in Table 5. It can be observed that applying our optimization strategy to the PromptIR [29] architecture yields a 0.97 dB improvement in PSNR. Compared with continual learning, our optimization strategy improves UniRain by 1.69 dB in PSNR, highlighting its effectiveness.

Table 4. Ablation analysis for RAG-based dataset distillation.

Variants	only VLM	w/o Retrieval stage	w/o Generation stage	UniRain (Ours)
PSNR \uparrow	27.73	28.39	28.36	28.93
SSIM \uparrow	0.8358	0.8453	0.8425	0.8515

Table 5. Ablation analysis on various models using different optimizers, including our adaptive reweighting optimization strategy.

Base Models	Optimization Strategy			Metrics	
	Continual learning	Prompt learning	Ours	PSNR \uparrow	SSIM \uparrow
PIGWM [55]	\checkmark	\times	\times	18.38	0.5758
	\times	\times	\checkmark	18.68	0.5880
PromptIR [29]	\times	\checkmark	\times	18.58	0.5639
	\times	\times	\checkmark	19.55	0.5759
UniRain (Ours)	\checkmark	\times	\times	18.92	0.5679
	\times	\checkmark	\times	19.64	0.5737
	\times	\times	\checkmark	20.61	0.5881

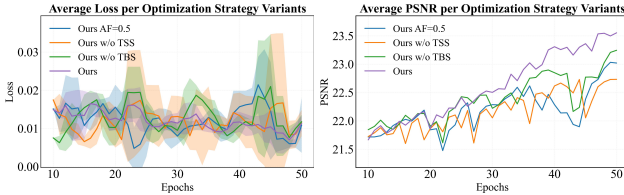


Figure 7. Loss and PSNR of the optimization strategy variants.

To disentangle the interplay between the effectiveness of optimization strategies and that of models, we further analyze the effect of different models under the same optimization strategy. As shown in Table 5, under the same prompt-learning optimization setting, UniRain achieves a 1.06 dB gain in PSNR over PromptIR [29]. Moreover, under the same multi-objective reweighted optimization strategy, it surpasses PIGWM [55] by 2.23 dB in PSNR metric.

Finally, we investigate the influence of different variants of the optimization strategy, including (i) a fixed adaptive factor ($AF = 0.5$), (ii) removing the task stability score (w/o TSS), and (iii) removing the task balance score (w/o TBS). As illustrated in Figure 7a, the average loss curves indicate that our full strategy achieves more stable optimization throughout training. Meanwhile, the average PSNR results in Figure 7b confirm that our complete formulation enables faster convergence and higher overall performance compared with the ablated variants.

Effectiveness of asymmetric MoE architecture. To validate the effectiveness of asymmetric MoE architecture, we conduct ablation studies as shown in Table 6. The baseline model without any MoE modules yields the lowest performance, indicating that a plain backbone cannot effectively model complex and diverse rain degradations. Introducing hard-MoE in both the encoder and decoder significantly enhances performance. In contrast, using soft-MoE in both stages leads to performance degradation, suggesting that soft routing alone is insufficient to capture heterogeneous degradations. Our design adopts soft-MoE in the encoder for exhaustive expert exploration and hard-MoE in the decoder for selective expert activation, and their integration

Table 6. Ablation analysis of asymmetric MoE architecture. Experiments are conducted on the proposed RainRAG dataset.

Variants	Encoder		Decoder		Metrics	
	hard-MoE	soft-MoE	hard-MoE	soft-MoE	PSNR \uparrow	SSIM \uparrow
Baseline	\times	\times	\times	\times	27.54	0.8442
Variant 1	\checkmark	\times	\checkmark	\times	28.39	0.8471
Variant 2	\checkmark	\times	\times	\checkmark	28.15	0.8485
Variant 3	\times	\checkmark	\times	\checkmark	27.91	0.8465
UniRain (Ours)	\times	\checkmark	\checkmark	\times	28.93	0.8515

Table 7. Extension to all-in-one weather restoration on the WeatherBench dataset [14], which contains real-world multi-weather degradations (rain, snow, and haze). Average results are reported.

Methods	TransWeather [38]	WGWS-Net [56]	Histoformer [37]	UniRain (Ours)
PSNR \uparrow	24.70	23.89	24.59	26.01
SSIM \uparrow	0.7931	0.7811	0.7976	0.8032

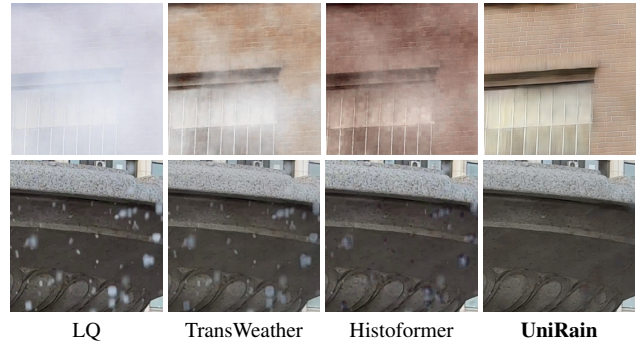


Figure 8. Visual comparison of all-in-one weather restoration results (e.g., hazy input (first row) and snowy input (second row)).

enables the model to achieve the best overall performance.

Extension to all-in-one weather restoration. We extend our network to all-in-one weather restoration and compare it with adverse weather restoration method (i.e., TransWeather [38]) and all-in-one image restoration approaches (i.e., WGWS-Net [56], and Histoformer [37]). Table 7 and Figure 8 show that our framework achieves a clear quantitative advantage and better visual restoration results, demonstrating its effectiveness in all-in-one weather restoration.

5. Conclusion

We have presented an effective unified framework for image deraining, called UniRain, which addresses rain streak and raindrop degradations under both daytime and nighttime conditions. We construct an intelligent retrieval augmented generation-based dataset distillation pipeline to better improve model generalization, enabling mixed training with high-quality samples distilled from existing deraining datasets. To achieve consistent performance and improved robustness across diverse scenarios, we integrate a simple yet effective multi-objective reweighted optimization strategy into the asymmetric union-of-experts architecture. Extensive experiments show that our method achieves competitive performance compared with state-of-the-art models on both our proposed benchmarks and multiple public datasets.

References

- [1] Yunhao Ba, Howard Zhang, Ethan Yang, Akira Suzuki, Arnold Pfahnl, Chethan Chinder Chandrappa, Celso M De Melo, Suyu You, Stefano Soatto, Alex Wong, et al. Not just streaks: Towards ground truth for single image deraining. In *ECCV*, 2022. 1, 2, 5
- [2] Andreas Blattmann, Robin Rombach, Kaan Oktay, Jonas Müller, and Björn Ommer. Semi-parametric neural image synthesis. *arXiv preprint arXiv:2204.11824*, 2022. 2
- [3] Wenhui Chang, Hongming Chen, Xin He, Xiang Chen, and Liangduo Shen. Uav-rain1k: A benchmark for raindrop removal from uav aerial imagery. In *CVPRW*, 2024. 5
- [4] Hongming Chen, Xiang Chen, Jiyang Lu, and Yufeng Li. Rethinking multi-scale representations in deep deraining transformer. In *AAAI*, 2024. 1, 5, 6, 7
- [5] Xiang Chen, Hao Li, Mingqiang Li, and Jinshan Pan. Learning a sparse transformer network for effective image deraining. In *CVPR*, 2023. 5, 6, 7
- [6] Xiang Chen, Jinshan Pan, and Jiangxin Dong. Bidirectional multi-scale implicit neural representations for image deraining. In *CVPR*, 2024. 5, 6, 7
- [7] Xiang Chen, Jinshan Pan, Jiangxin Dong, and Jinhui Tang. Towards unified deep image deraining: A survey and a new benchmark. *IEEE TPAMI*, 2025. 2
- [8] Zhe Chen, Weiyun Wang, Yue Cao, Yangzhou Liu, Zhangwei Gao, Erfei Cui, Jinguo Zhu, Shenglong Ye, Hao Tian, Zhaoyang Liu, et al. Expanding performance boundaries of open-source multimodal models with model, data, and test-time scaling. *arXiv preprint arXiv:2412.05271*, 2024. 4
- [9] Michael Crawshaw. Multi-task learning with deep neural networks: A survey. *arXiv preprint arXiv:2009.09796*, 2020. 3
- [10] Yunfan Gao, Yun Xiong, Xinyu Gao, Kangxiang Jia, Jintian Liu, Yuxi Bi, Yixin Dai, Jiawei Sun, Haofen Wang, and Haofen Wang. Retrieval-augmented generation for large language models: A survey. *arXiv preprint arXiv:2312.10997*, 2023. 2
- [11] Zi Gong, Hang Yu, Cong Liao, Bingchang Liu, Chaoyu Chen, and Jianguo Li. Cobra: convergence balancer for multi-task finetuning of large language models. *arXiv preprint arXiv:2410.06741*, 2024. 2, 4
- [12] Maarten Grootendorst. Keybert: Minimal keyword extraction with bert., 2020. 3
- [13] Qiyuan Guan, Xiang Chen, Guiyue Jin, Jiyu Jin, Shumin Fan, Tianyu Song, and Jinshan Pan. Rethinking nighttime image deraining via learnable color space transformation. *NeurIPS*, 2025. 1, 2, 5
- [14] Qiyuan Guan, Qianfeng Yang, Xiang Chen, Tianyu Song, Guiyue Jin, and Jiyu Jin. Weatherbench: A real-world benchmark dataset for all-in-one adverse weather image restoration. In *ACM MM*, 2025. 5, 7, 8
- [15] Hang Guo, Tao Dai, Zhihao Ouyang, Taolin Zhang, Yaohua Zha, Bin Chen, and Shu-tao Xia. Refir: Grounding large restoration models with retrieval augmentation. *NeurIPS*, 2024. 2
- [16] Yun Guo, Xueyao Xiao, Yi Chang, Shumin Deng, and Luxin Yan. From sky to the ground: A large-scale benchmark and simple baseline towards real rain removal. In *ICCV*, 2023. 1, 2, 5
- [17] Kui Jiang, Zhongyuan Wang, Peng Yi, Chen Chen, Baojin Huang, Yimin Luo, Jiayi Ma, and Junjun Jiang. Multi-scale progressive fusion network for single image deraining. In *CVPR*, 2020. 1, 2, 5
- [18] Kui Jiang, Zhongyuan Wang, Peng Yi, Chen Chen, Zheng Wang, Xiao Wang, Junjun Jiang, and Chia-Wen Lin. Rain-free and residue hand-in-hand: A progressive coupled network for real-time image deraining. *IEEE TIP*, 2021. 1
- [19] Zhiqiang Kou, Jing Wang, Yuheng Jia, and Xin Geng. Progressive label enhancement. *PR*, 2025. 1
- [20] M Kumar, Benjamin Packer, and Daphne Koller. Self-paced learning for latent variable models. *NeurIPS*, 2010. 3
- [21] Patrick Lewis, Ethan Perez, Aleksandra Piktus, Fabio Petroni, Vladimir Karpukhin, Naman Goyal, Heinrich Küttler, Mike Lewis, Wen-tau Yih, Tim Rocktäschel, et al. Retrieval-augmented generation for knowledge-intensive nlp tasks. *NeurIPS*, 2020. 2
- [22] Feng Li, Renrui Zhang, Hao Zhang, Yuanhan Zhang, Bo Li, Wei Li, Zejun Ma, and Chunyuan Li. Llava-next-interleave: Tackling multi-image, video, and 3d in large multimodal models. *arXiv preprint arXiv:2407.07895*, 2024. 4
- [23] Hao Li, Xiang Chen, Jiangxin Dong, Jinhui Tang, and Jinshan Pan. Foundir: Unleashing million-scale training data to advance foundation models for image restoration. In *ICCV*, 2025. 1
- [24] Junnan Li, Dongxu Li, Caiming Xiong, and Steven Hoi. Bliip: Bootstrapping language-image pre-training for unified vision-language understanding and generation. In *ICML*, 2022. 3
- [25] Pengpeng Li, Xiangbo Shu, Chun-Mei Feng, Yifei Feng, Wangmeng Zuo, and Jinhui Tang. Surgical video workflow analysis via visual-language learning. *npj Health Systems*, 2025. 2
- [26] Wei Li, Qiming Zhang, Jing Zhang, Zhen Huang, Xinmei Tian, and Dacheng Tao. Toward real-world single image deraining: A new benchmark and beyond. *arXiv preprint arXiv:2206.05514*, 2022. 5, 7
- [27] Shih-Jui Liang, Zihao Chen, Jun-Cheng Chen, and Yan-Tsung Peng. Enhancing image deraining through vlm-based data refinement and classification. In *ICIP*, 2025. 2
- [28] Avideep Mukherjee, Soumya Banerjee, Piyush Rai, and Vinay P Namboodiri. Rissole: Parameter-efficient diffusion models via block-wise generation and retrieval-guidance. *arXiv preprint arXiv:2408.17095*, 2024. 2
- [29] Vaishnav Potlapalli, Syed Waqas Zamir, Salman H Khan, and Fahad Shahbaz Khan. Promptir: Prompting for all-in-one image restoration. *NeurIPS*, 2023. 7, 8
- [30] Rui Qian, Robby T Tan, Wenhan Yang, Jiajun Su, and Jiaying Liu. Attentive generative adversarial network for raindrop removal from a single image. In *CVPR*, 2018. 1, 2, 5
- [31] Ruijie Quan, Xin Yu, Yuanzhi Liang, and Yi Yang. Removing raindrops and rain streaks in one go. In *CVPR*, 2021. 1, 2, 5, 6, 7

- [32] Alec Radford, Jong Wook Kim, Chris Hallacy, Aditya Ramesh, Gabriel Goh, Sandhini Agarwal, Girish Sastry, Amanda Askell, Pamela Mishkin, Jack Clark, et al. Learning transferable visual models from natural language supervision. In *ICML*, 2021. 3
- [33] Dongwei Ren, Wangmeng Zuo, Qinghua Hu, Pengfei Zhu, and Deyu Meng. Progressive image deraining networks: A better and simpler baseline. In *CVPR*, 2019. 5, 6, 7
- [34] Aleksandrs Slivkins et al. Introduction to multi-armed bandits. *FTML*, 2019. 3
- [35] Tianyu Song, Guiyue Jin, Pengpeng Li, Kui Jiang, Xiang Chen, and Jiyu Jin. Learning a spiking neural network for efficient image deraining. *arXiv preprint arXiv:2405.06277*, 2024. 1
- [36] Lingchen Sun, Jie Liang, Shuaizheng Liu, Hongwei Yong, and Lei Zhang. Perception-distortion balanced super-resolution: A multi-objective optimization perspective. *IEEE TIP*, 2024. 3
- [37] Shangquan Sun, Wenqi Ren, Xinwei Gao, Rui Wang, and Xiaochun Cao. Restoring images in adverse weather conditions via histogram transformer. In *ECCV*, 2024. 8
- [38] Jeya Maria Jose Valanarasu, Rajeev Yasarla, and Vishal M Patel. Transweather: Transformer-based restoration of images degraded by adverse weather conditions. In *CVPR*, 2022. 8
- [39] Hong Wang, Qi Xie, Qian Zhao, and Deyu Meng. A model-driven deep neural network for single image rain removal. In *CVPR*, 2020. 5, 6, 7
- [40] Tianyu Wang, Xin Yang, Ke Xu, Shaozhe Chen, Qiang Zhang, and Rynson WH Lau. Spatial attentive single-image deraining with a high quality real rain dataset. In *CVPR*, 2019. 2, 5
- [41] Zhenwei Wang, Tengfei Wang, Zexin He, Gerhard Hancke, Ziwei Liu, and Rynson WH Lau. Phidias: A generative model for creating 3d content from text, image, and 3d conditions with reference-augmented diffusion. *arXiv preprint arXiv:2409.11406*, 2024. 2
- [42] Qiang Wen, Yue Wu, and Qifeng Chen. Video waterdrop removal via spatio-temporal fusion in driving scenes. In *ICRA*, 2023. 5
- [43] Qinzhuo Wu, Weikai Xu, Wei Liu, Tao Tan, Jianfeng Liu, Ang Li, Jian Luan, Bin Wang, and Shuo Shang. Mobilevlm: A vision-language model for better intra-and inter-ut understanding. *arXiv preprint arXiv:2409.14818*, 2024. 4
- [44] Jie Xiao, Xueyang Fu, Aiping Liu, Feng Wu, and Zheng-Jun Zha. Image de-raining transformer. *IEEE TPAMI*, 2022. 5, 6, 7
- [45] Hujie Yan. Towards universal rainy image restoration: Benchmark and baseline. In *AAAI*, 2025. 1, 2, 5, 6, 7
- [46] An Yang, Baosong Yang, Beichen Zhang, Binyuan Hui, Bo Zheng, Bowen Yu, Chengyuan Li, Dayiheng Liu, Fei Huang, Haoran Wei, Huan Lin, Jian Yang, Jianhong Tu, Jianwei Zhang, Jianxin Yang, Jiayi Yang, Jingren Zhou, Junyang Lin, Kai Dang, Keming Lu, Keqin Bao, Kexin Yang, Le Yu, Mei Li, Mingfeng Xue, Pei Zhang, Qin Zhu, Rui Men, Runji Lin, Tianhao Li, Tingyu Xia, Xingzhang Ren, Xuancheng Ren, Yang Fan, Yang Su, Yichang Zhang, Yu Wan, Yuqiong Liu, Zeyu Cui, Zhenru Zhang, and Zihan Qiu. Qwen2.5 technical report. *arXiv preprint arXiv:2412.15115*, 2024. 3
- [47] Qianfeng Yang, Xiang Chen, Pengpeng Li, Qiyuan Guan, Guiyue Jin, and Jiyu Jin. Rethinking rainy 3d scene reconstruction via perspective transforming and brightness tuning. *arXiv preprint arXiv:2511.06734*, 2025. 2
- [48] Wenhan Yang, Robby T Tan, Jiashi Feng, Jiaying Liu, Zongming Guo, and Shuicheng Yan. Deep joint rain detection and removal from a single image. In *CVPR*, 2017. 1, 2, 5
- [49] Tianhe Yu, Saurabh Kumar, Abhishek Gupta, Sergey Levine, Karol Hausman, and Chelsea Finn. Gradient surgery for multi-task learning. *NeurIPS*, 2020. 3
- [50] Syed Waqas Zamir, Aditya Arora, Salman Khan, Munawar Hayat, Fahad Shahbaz Khan, Ming-Hsuan Yang, and Ling Shao. Multi-stage progressive image restoration. In *CVPR*, 2021. 5, 6, 7
- [51] Syed Waqas Zamir, Aditya Arora, Salman Khan, Munawar Hayat, Fahad Shahbaz Khan, and Ming-Hsuan Yang. Restormer: Efficient transformer for high-resolution image restoration. In *CVPR*, 2022. 5, 6, 7
- [52] Fan Zhang, Shaodi You, Yu Li, and Ying Fu. Gtav-nightrain: Photometric realistic large-scale dataset for night-time rain streak removal. *arXiv preprint arXiv:2210.04708*, 2022. 1, 2, 5
- [53] Fan Zhang, Shaodi You, Yu Li, and Ying Fu. Learning rain location prior for nighttime deraining. In *ICCV*, 2023. 5, 6, 7
- [54] Zilun Zhang, Haozhan Shen, Tiancheng Zhao, Zian Guan, Bin Chen, Yuhao Wang, Xu Jia, Yuxiang Cai, Yongheng Shang, and Jianwei Yin. Imagerag: Enhancing ultra high resolution remote sensing imagery analysis with imagerag. *arXiv preprint arXiv:2411.07688*, 2024. 2
- [55] Man Zhou, Jie Xiao, Yifan Chang, Xueyang Fu, Aiping Liu, Jinshan Pan, and Zheng-Jun Zha. Image de-raining via continual learning. In *CVPR*, 2021. 7, 8
- [56] Yurui Zhu, Tianyu Wang, Xueyang Fu, Xuanyu Yang, Xin Guo, Jifeng Dai, Yu Qiao, and Xiaowei Hu. Learning weather-general and weather-specific features for image restoration under multiple adverse weather conditions. In *CVPR*, 2023. 8